

Water Resources Research

RESEARCH ARTICLE

10.1029/2019WR025146

Key Points:

- Spatial distributions of (im)permeable areas along flowpaths often determine hill slope hydrology
- A machine learning emulator rapidly predicts infiltration and velocity fields across arbitrary impermeable and permeable surface patterns
- The spatial features controlling hydrological function vary with storm, slope, and soil properties

Supporting Information:

- Supporting Information S1
- Figure S1
- Figure S2
- Figure S3
- Figure S4
- Figure S5
- Figure S6
- Figure S7
- Figure S8
- Figure S9
- Figure S10
- Figure S11
- Figure S12
- Figure S13

Correspondence to:

O. Crompton,
octavia@berkeley.edu

Citation:

Crompton, O. V., Sytsma, A., & Thompson, S. (2019). Emulation of the Saint Venant equations enables rapid and accurate predictions of infiltration and overland flow velocity on spatially heterogeneous surfaces. *Water Resources Research*, 55, 7108–7129. <https://doi.org/10.1029/2019WR025146>

Received 13 MAR 2019

Accepted 31 JUL 2019

Accepted article online 6 AUG 2019

Published online 22 AUG 2019

Emulation of the Saint Venant Equations Enables Rapid and Accurate Predictions of Infiltration and Overland Flow Velocity on Spatially Heterogeneous Surfaces

Octavia Crompton^{1,2} , Anneliese Sytsma³ , and Sally Thompson^{2,4} 

¹Department of Earth and Planetary Science, University of California, Berkeley, CA, USA, ²Department of Civil and Environmental Engineering, University of California, Berkeley, CA, USA, ³Department of Landscape Architecture and Environmental Planning, University of California, Berkeley, CA, USA, ⁴Department of Environmental Engineering, University of Western Australia, Perth, Western Australia, Australia

Abstract The interleaving of impermeable and permeable surfaces along a runoff flow path controls the hillslope hydrograph, the spatial pattern of infiltration, and the distribution of flow velocities in landscapes dominated by overland flow. Predictions of the relationship between the pattern of (im)permeable surfaces and hydrological outcomes tend to fall into two categories: (i) generalized metrics of landscape pattern, often referred to as connectivity metrics, and (ii) direct simulation of specific hillslopes. Unfortunately, the success of using connectivity metrics for prediction is mixed, while direct simulation approaches are computationally expensive and hard to generalize. Here we present a new approach for prediction based on emulation of a coupled Saint Venant equation-Richards equation model with random forest regression. The emulation model predicts infiltration and peak flow velocities for every location on a hillslope with an arbitrary spatial pattern of impermeable and permeable surfaces but fixed soil, slope, and storm properties. It provides excellent fidelity to the physically based model predictions and is generalizable to novel spatial patterns. The spatial pattern features that explain most of the hydrological variability are not stable across different soils, slopes, and storms, potentially explaining some of the difficulties associated with direct use of spatial metrics for predicting landscape function. Although the current emulator relies on strong assumptions, including smooth topography, binary permeability fields, and only a small collection of soils, slope, and storm scenarios, it offers a promising way forward for applications in dryland and urban settings and in supporting the development of potential connectivity indices.

1. Introduction

The partitioning of rainfall between infiltration and runoff at the land surface (Horton, 1933) strongly determines the hydrological behavior of the urban, montane, agricultural, and desert landscapes in which infiltration excess (Hortonian) overland flow predominates (Descroix et al., 2007; Fletcher et al., 2013; Leopold, 1968). In these landscapes, however, the permeability of the land surface often varies along a flow path, so that relatively impermeable surfaces that generate overland flow (e.g., roads, roofs, and sidewalks in urban landscapes, Leopold, 1968; rocks in mountain areas; or crusted or sealed bare soil surfaces in drylands, Assouline, 2004; Belnap, 2006) are interleaved with more permeable, and often vegetated, areas with higher infiltration capacity (Thompson et al., 2010). The infiltration capacities of these (im)permeable surfaces, their relative size, and their arrangement along a flow path determines whether overland runoff reaches downslope channels, stormwater inlet structures, or other drainage features (Assouline et al., 2015) or instead mostly infiltrates into the subsurface. Consequently, the spatial pattern of permeability in surface runoff-producing landscapes determines (i) the total volume, timing, and velocity of storm hydrographs (Hoffman et al., 2017); (ii) the peak flow velocities that occur on the land surface and, thus, for example, the risk of surface erosion (Govers, 1992); and (iii) the water balance and distribution of infiltrated water volumes through space and, thus, for example, the spatial pattern of plant available water (Hoffman et al., 2017). Therefore, whether managers or environmental designers wish to maximize plant water availability and minimize degradation risks in drylands, to reduce peak flows and extend baseflows in urban streams, to combat the urban heat island effect by maximizing vegetation transpiration, or to limit soil erosion in agricultural systems, or any number of other water balance- or flow-related environmental outcomes, they

must confront the question of how the spatial organization of land surface permeability impacts runoff and water balance partitioning within and at the hillslope scale.

Attempts to answer this question fall into two areas: (i) development of “connectivity” indicators (Okin et al., 2015; Turnbull et al., 2018) and (ii) direct simulation of specific landscapes. Connectivity indicators attempt to generalize the problem by identifying metrics of landscape pattern (or function) that predict the fraction of the hillslope that generates runoff and routes it to an outlet. Examples of such metrics include the fractional cover of (im)permeable surfaces (Arnold & Gibbons, 1996; Schueler et al., 2009; Shuster et al., 2005) and related concepts such as “geodiversity” (Stavi et al., 2018), patch size distributions of each type of surface (Alberti et al., 2007; Turner, 1989), graph theoretic or network measures (Masselink et al., 2017), contiguity indices (Ludwig et al., 2007; Mayor et al., 2008), and connected impervious surface area (relating to the area of impermeable surface that lies directly upslope from an outlet with no intervening permeable areas; Alley & Veenhuis, 1983; Booth & Jackson, 1997; Lee & Heaney, 2003; Leopold, 1968). Note that in this study, for simplicity, we label all hillslope-scale spatial descriptors of the (im)permeable surface patchiness as “connectivity metrics.” The appeal of connectivity metrics lies in the ease with which land cover (as a surrogate for permeability) can be observed from aerial imagery, allowing the metrics to be readily computed (e.g., within Geographic Information System packages), and the simple and ideally generalizable nature of these metrics across multiple landscapes to inform analysis or design. Connectivity metrics, however, do not always provide a clear predictive basis for hydrological function. This is potentially because they represent connectivity of the spatial features of a landscape, or “static connectivity” (Bracken & Croke, 2007), which do not always map clearly to hydrologic function. Connectivity metrics that represent within-storm states of water distribution, or “functional connectivity” (Bracken et al., 2013; Bracken & Croke, 2007), may be more suitable for estimation of hydrologic function; however, such metrics are difficult to quantify and predict (Larsen et al., 2012; Okin et al., 2015).

Direct simulation of runoff and infiltration on specific landscapes provides an alternative, although less general, approach to capturing the effects of spatial patterns of permeability on hydrologic function. Sheet flow during storm events typically results in shallow flows (<5 cm), which can locally vary in depth and velocity, as water passes over surfaces of variable permeability. Such shallow, unsteady, and heterogeneous flows are well represented by the Saint Venant equations (SVE) or “shallow water equations” (Brutsaert, 2005), which in two dimensions take the following form:

$$\frac{\partial h}{\partial t} + \frac{\partial(Uh)}{\partial x} + \frac{\partial(Vh)}{\partial y} = p - i \quad (1)$$

$$\frac{\partial U}{\partial t} + U \frac{\partial U}{\partial x} + V \frac{\partial U}{\partial y} + g \frac{\partial h}{\partial x} + g(S_{fx} - S_x) + \frac{U(p - i)}{h} = 0 \quad (2)$$

$$\frac{\partial V}{\partial t} + U \frac{\partial V}{\partial x} + V \frac{\partial V}{\partial y} + g \frac{\partial h}{\partial y} + g(S_{fy} - S_y) + \frac{V(p - i)}{h} = 0 \quad (3)$$

where U , V denote the depth-averaged flow velocities in the x and y directions, respectively; h is the depth of flow; S_x and S_y are the bed slope in the x and y directions; t is time; and g represents gravitational acceleration. The terms S_{fx} and S_{fy} are the x and y components of the friction slope (or energy gradient), which represent the effect of bed and other shear stresses on retarding the flow and are typically represented by empirical friction formulae (Smith et al., 2007). Rainfall inputs (p) and infiltration losses (i) add or remove mass from the system but are assumed to have a negligible impact on local momentum transfers.

A variety of models are available to solve the SVE or simplifications to them, on landscapes with variable permeability. These include the connectivity of runoff model (Reaney et al., 2007), Gridded Surface Subsurface Hydrologic Analysis model (e.g., Fry & Maxwell, 2017), ParFlow (e.g., Bhaskar et al., 2015), and bespoke solutions of the overland flow equations (Mügler et al., 2011; Thompson et al., 2011). Though these models provide detailed understanding of specific hillslope environments, they require modeling expertise and are computationally demanding. These hurdles prevent nonexpert modelers from easily using these tools and restrict modelers to using only a small number of simulations.

Emulation (also known as surrogate-based or meta-) models provide a third approach that retains the fidelity of predictions made in specific landscapes while reducing the computational burden of solving the physi-

cal flow equations. An emulator, loosely defined, is “a model of a model” that replaces a computationally intensive process model with an accurate but simplified model structure that is much faster to solve (Castelletti et al., 2012; Razavi et al., 2012; Rohmer et al., 2018). Emulation modeling approaches are widely used to replace computationally expensive process models when numerous simulations are required, in circumstances including model calibration, sensitivity analysis, forecasting, and optimization (Castelletti et al., 2012; Razavi et al., 2012). They can be created in numerous ways, for instance, by simplifying a process model’s structure or by fitting a data model (e.g., a regression, kriging, spline, or machine learning method) to simulation output from the process model (Castelletti et al., 2012; García-Alba et al., 2018). Emulation models are not specific in their application to any one field and in environmental contexts have been used to represent groundwater flow (Kumar et al., 2010; Rogers & Dowla, 1994; Yan & Minsker, 2003), water distribution networks, surface water systems (Bhattacharjya & Datta, 2005; Broad et al., 2005; Castelletti et al., 2010; Neelakantan & Pundarikanthan, 2000; Sreekanth & Datta, 2010), and agricultural systems (Audsley et al., 2008; Børgesen et al., 2001; Garcet et al., 2006), among others. To date, however, emulation models have not been applied to the problem of predicting how spatial patterns of surface permeability determine hillslope hydrological function.

Here, we use a machine learning approach—random forest regression—to emulate the predictions of a SVE model for infiltration excess overland flow on a planar hillslope covered in a two-phase mosaic of (im)permeable surfaces. Random forest regression involves averaging over an ensemble of decision trees (a “forest”), each of which is fit to approximately two thirds of the modeled data (with the two thirds selected at random; Breiman, 2001). Random forests are relatively easy to train, are fast to execute (Breiman, 2001), and, in our preliminary analyses, outperformed alternative machine learning techniques (K-nearest neighbors, support vector machines, neural networks, and multivariate linear regression) for emulating solutions to the SVE.

The research presented here has three main objectives. First, it aims to train an ensemble of emulators that can replace the SVE when predicting spatial fields of cumulative infiltration I and maximum (end of storm) flow velocity U_{\max} for any spatial pattern of (im)permeable surface patches.

Second, it assesses the generalizability of the emulators to “novel” patterns that are distinct from those on which the emulators were fit. To do this, the emulator performance is assessed when predicting hydrological outcomes for test data sets that (i) impose anisotropy on patterns that are otherwise similar to those used to train the emulator, and (ii) draw on “real world” spatial patterns from suburban landscapes.

Finally, it presents a case study that illustrates the value of the emulator methodology, using it to generate many predictions of hillslope-scale infiltration fraction IF for different patterns, rainstorms, hillslopes, and soil characteristics. The infiltration fraction is the ratio of the hillslope-mean infiltration depth to the rainfall depth and is used to represent an example of hillslope hydrological function. The resulting large data set is used to evaluate the predictive value of simple spatial metrics, such as connectivity metrics, in explaining variations in IF .

The approach adopted here requires training a separate random forest for each combination of storm and hillslope properties. Although this means that the emulators are not generalized for all conditions, it nonetheless represents an enormous simplification, relative to requiring specific simulations for all possible patterns. For example, on the 1-m² resolution 100 × 50-m slopes used in this study, there are $\mathcal{O}(10^{1,500})$ possible ways to organize a binary spatial arrangement of surface types. Although we do not attempt further generalization of our predictions to arbitrary soil, slope, and storm properties in this study, we discuss how such generalization could be achieved in section 4.3.

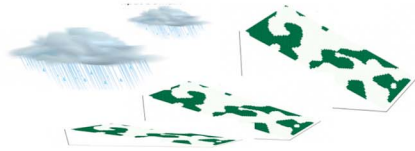
2. Methods

2.1. Overview

The study proceeded in four main steps, shown schematically in Figure 1 and described below. The first step was to generate the data on which the emulators were trained. This step, described in section 2.2, used a bespoke solver for the SVE to generate the overland flow and infiltration data to which the emulators were fit. The next step was a model and feature selection process, which identified the features on which individual random forest models were trained, as outlined in section 2.3. The models were then tuned to improve their performance (section 2.4), using a cross-validation approach to minimize errors. Section 2.5 describes the performance of the emulators when applied to a novel and distinct set of spatial (im)permeability patterns.

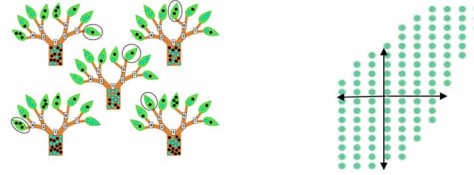
1. Data Generation

Run SVE model on randomly generated isotropic patterns, for a multiple landscape/storm scenarios.



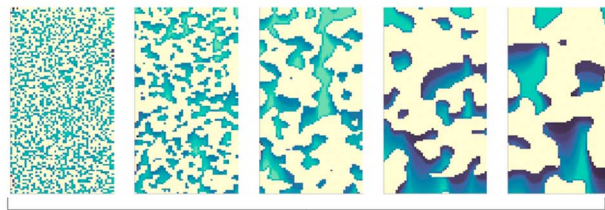
2. Emulator Model Selection

Select random forest regression and 'core' features based on exploratory analysis.



3. Emulator Model Tuning

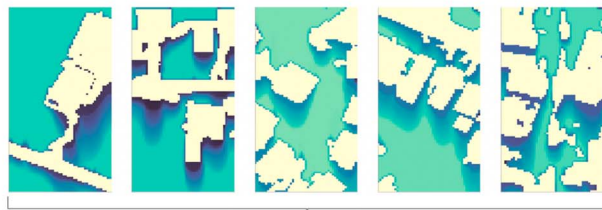
Adjust RF max depth and feature smoothing to minimize validation errors, using k-fold cross-validation.



Isotropic training/validation set

4. Model Generalizability

Assess model performance on "novel" patterns, using the emulators fit to the isotropic patterns.



Anisotropic and suburban test sets

Figure 1. Steps involved in constructing, validating, and generalizing the emulators. "Data Generation" involved bespoke solutions of the SVE for a broad range of landscape, storm, and soil scenarios. "Model Selection" involved choosing an appropriate machine learning algorithm and engineering features to represent the domain around each figure. "Model Tuning" refers to minimizing the cross-validation errors by adjusting the random forest maximum depth and smoothing the features using k-fold cross validation. Finally, "Model Generalizability" assessed the performance of the emulators when applied to novel (anisotropic and suburban-derived) spatial patterns. SVE = Saint Venant equation.

Finally, the emulators were interpreted in terms of the spatial features having the greatest importance for the infiltration and overland flow outcomes (section 2.6).

2.2. Data Generation

The use of any data modeling approach for emulation requires generating data on which the model can be trained and tested. Here these data consisted of solutions of the SVE model for multiple spatial fields of (im)permeable surfaces, occurring for different landscape and storm characteristics.

2.2.1. SVE Model

Solving the SVEs on permeable landscapes requires specifying the terms p and i in equations (1)–(3). We represented rainfall p with its storm-averaged intensity, which was treated as a constant for each simulation. The infiltration rate i was represented by coupling the Richards equation (Richards, 1931) to the SVE solver at each time step. We considered infiltration in one dimension (vertical, z) only, which is appropriate for the short time scales and relatively shallow slopes addressed in this problem. The one-dimensional (vertical) Richards equation is given by

$$\frac{\partial \theta}{\partial t} = \frac{\partial}{\partial z} \left[K(\theta) \left(\frac{\partial H}{\partial z} + 1 \right) \right] \quad (4)$$

where $K(\theta)$ is the hydraulic conductivity, H the matric head, z the elevation above a vertical datum, and θ the volumetric water content. The first term on the right-hand side of the equation represents the effects of capillarity, and the second term represents those of gravity-driven flux (Farthing & Ogden, 2017). To use Richards equation, the water content θ must be related to the head H . Here we used the Van Genuchten (1980) equation to describe this relationship:

$$\theta(H) = \theta_R + \frac{\theta_S - \theta_R}{[1 + (\alpha|H|)^s]^{1-1/s}} \quad (5)$$

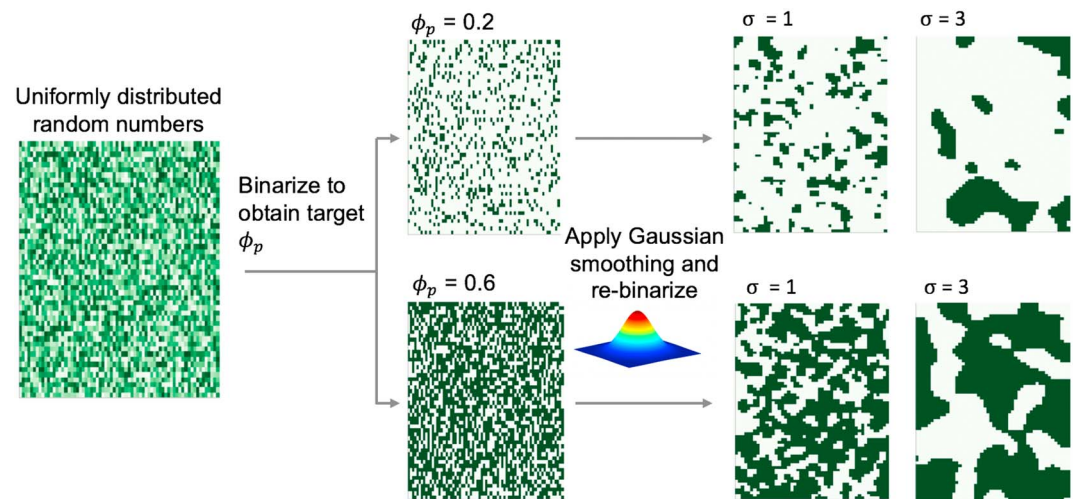


Figure 2. Patterns were randomly generated from arrays of random numbers between 0 and 1, which were binarized to obtain the nonsmoothed ($\sigma = 0$) spatial pattern. For each pattern, the target permeable fraction, ϕ_p , was achieved by adjusting the threshold value used to binarize the array. Colors indicate contrasting permeability: Green areas are permeable, white impermeable. The patch length scale was adjusted by applying a Gaussian filter to the binary patterns and rebinarizing to preserve the desired ϕ_p . The standard deviation of the Gaussian kernel σ determines the characteristic patch length scale.

where θ_s and θ_R are the saturated and residual soil water content, respectively, s is a measure of the pore size distribution in the soil, and α parameterizes the air entry pressure. Richards equation is applied between the soil surface and a free drainage (zero gradient) bottom boundary.

The SVE and Richards equation were coupled at the soil surface via the boundary conditions on infiltration: a Dirichlet boundary condition with $H =$ the ponded depth where surface ponding occurs and a Neumann boundary condition that sets $i = p + Q_{in}$, where Q_{in} is any net inflow from runoff, in the absence of ponding. The equations were then solved with two previously validated methods: a finite volume model for the SVE developed by Bradford and Katopodes (1999) and the Celia et al. (1990) mass-conserving one-dimensional algorithm for Richards equation. The Bradford and Katopodes (1999) method uses the monotone upstream scheme for conservation laws to achieve second-order spatial accuracy, in conjunction with predictor-corrector time stepping to provide a second-order accurate solution. The Celia et al. (1990) algorithm is a standard numerical approach, used in many unsaturated flow codes such as Hydrus 1-D (Simunek et al., 2005). It involves a backward Euler implementation of the mixed $H - \theta$ formulation of Richards equation (Celia et al., 1990), with modified Picard iterations to improve mass conservation. Because the Richards equation solver was the more time-intensive component of the model, the overland flow and infiltration components were solved with different time steps to increase computational efficiency: 2 s for Richards equation and 0.2 ms for the SVE, to satisfy stability criteria. To check the coupling of the two model components, we verified that they correctly reproduced analytical solutions to the kinematic wave equation with infiltration (Giraldez & Woolhiser, 1996; see supporting information Text S1).

2.2.2. Pattern Generation and Selection

Many realizations of different spatial distributions of the (im)permeable areas on the land surface (referred to as “patterns”) were needed to train and validate the emulator models. We used random, spatial patterns with isotropic patch characteristics (i.e., the statistics describing patch length scales were not dependent on direction) on a 50×100 -m gridded domain consisting of 1×1 -m cells for this purpose. We drew a random number from a uniform distribution (0,1) for each grid cell. Cells with value $\geq \phi_p$, where ϕ_p was a prescribed permeable fraction of the landscape, were assigned a 0 value, and all other cells a 1. The binary domain was then convolved with a symmetrical bivariate Gaussian kernel with standard deviation σ and the results binarized to 0 or 1 around a threshold given by the ϕ_p percentile of the array (Jones et al., 2014). Multiple patterns were made to span a range of values in ϕ_p and σ , as illustrated in Figure 2 (note that in practice we generated new random arrays for each σ - ϕ_p combination, thus maximizing the variation in the patterns).

We anticipated that the similarity (e.g., Gaussian spatial structures) of training patterns produced in this way might limit the generalizability of the emulator to new patterns (and mean that performance metrics

Table 1
Parameters for the Coupled SVE-Richards Equation Model Simulations

Parameter	Description	Units	Values
n_I	Manning's n (impermeable)	$\text{s/m}^{1/3}$	0.03
n_P	Manning's n (permeable)	$\text{s/m}^{1/3}$	0.1
L_x, L_y	Domain size	m	100×50
dx	Grid resolution	m	1.0
Soil parameters			
s	Pore size distribution	—	1.47
α	van Genuchten parameter	—	$9.6\text{e}-3$
θ_S	Saturated soil moisture content	—	0.472
θ_R	Residual soil moisture content	—	0.0378
z_{max}	Soil depth	cm	20.0
H_0	Initial H	cm	-342.0
Scenario parameters			
p	Storm intensity	cm/hr	2.0, 8.0
t_{storm}	Storm duration	min	30.
K_S	Hydraulic conductivity (permeable areas)	cm/hr	2.0, 8.0
S_o	Hillslope gradient	%	2.0, 15.0
Training/validation pattern parameters			
ϕ_P	Permeable fraction	—	0.1, 0.2, ..., 0.9
σ	Patch length scale	—	0, 1, 2, 3, 4
Anisotropic pattern parameters			
ϕ_P	Permeable fraction	—	0.2, 0.4, 0.6, 0.8
(σ_x, σ_y)	x and y patch length scales	—	(1, 5), (3, 15), (5, 1), (15, 3)

Note. Where multiple parameter values are listed, the cases were run factorially.

obtained from patterns produced in a similar fashion might be positively biased compared to out-of-sample performance). For this reason, we modified the procedure above to create anisotropic patterns on which to test emulator performance. This was achieved by using a bivariate Gaussian kernel for smoothing, with σ_y and σ_x specified as the standard deviations of the kernel in the cross (y) and downslope (x) directions, respectively. Additionally, we obtained “real” test patterns from an impervious landcover data set for Sonoma County in Northern California (Mapping & LiDAR Program, 2016). We sampled 20 grids of 100×50 -m size with varying degrees of impervious surface cover. Images from each selected grid were clipped and regrid-ded to 1-m resolution. Examples of the anisotropic and suburban patterns are included in the supporting information (Figures S4 and S5). In total, we made three sets of patterns: isotropic training patterns consisting of (9) $\phi_P \times (5) \sigma$ combinations (45 total), anisotropic test patterns consisting of (4) $\phi_P \times (4) \sigma_x, \sigma_y$ (16 total), and suburban test patterns consisting of selected images (20 total; see Table 1 for details).

2.2.3. Data Generation for Specified Landscape and Storm Scenarios

The SVE and Richards equation models require specification of numerous parameters, most of which were held constant for all simulations as shown in Table 1. Soil infiltration (saturated hydraulic conductivity K_s) and roughness (Manning's n) were specified separately for impermeable and permeable cells, with higher roughness on permeable sites reflecting the common presence of vegetation. The boundary conditions for the simulation were a no-flux boundary condition (the hillslope divide) on the upslope boundary, an open (channel or other drainage) boundary at the downslope edge, and no-flux lateral boundaries. The domain was initialized without any surface ponding and with soils at field capacity.

With these features held constant, we developed eight scenarios, representing factorial combinations of two rainfall intensities ($p = 2.0$ and 8.0 cm/hr), two hillslope gradients ($S_o = 2$ and 15%), and two permeable-area infiltration capacities ($K_s = 2.0$ and 8.0 cm/hr) as summarized in Table 1 and illustrated in Figure 3 with sample infiltration maps for each scenario. These factorial combinations allow us to assess any sensitivities in the behavior and performance of the emulators as storm and landscape properties varied. The scenarios were combined with all the patterns described in section 2.2.2, yielding 360 (isotropic) training and 288 test

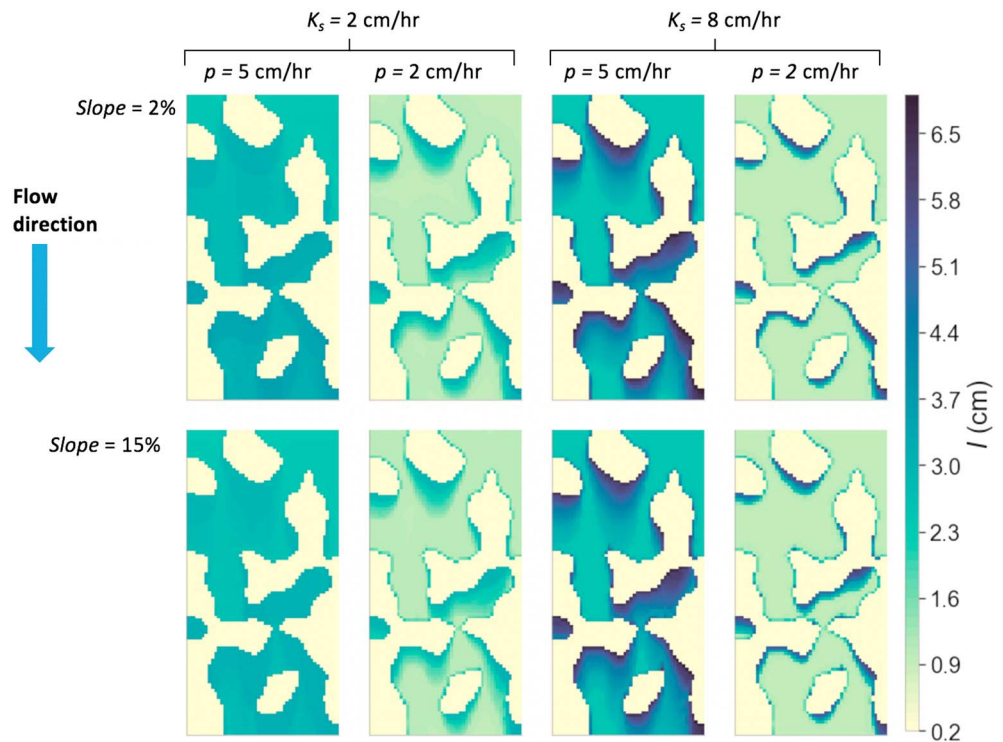


Figure 3. Infiltration maps for each scenario, for a sample spatial pattern. Dark colored areas are permeable, and light colored areas impermeable. Areas where runoff infiltrates downslope of where it is generated are visible as dark “edges” on the downslope boundary of the impermeable patches, and these are most pronounced with high rainfall rates p , steeper slopes, and high ratios of the conductivity K_s to the rainfall intensity p .

simulations (128 anisotropic and 160 suburban), representing all the runs of the coupled SVE and Richards equation models.

2.3. Emulator Model Selection

We expected that the emulator models would need to account for different dependencies on spatial patterns arising for each of (i) impermeable versus permeable cells, (ii) different target variables (I versus U_{\max}), and (iii) different soil, rainfall, and slope conditions (scenarios; e.g., Magliano et al., 2015). To account for this, we fit separate random forests for each cell type (impermeable or permeable), target variable (I or U_{\max}), and scenario, leading to the structure shown in Figure 4—an “ensemble” of emulators, consisting of an emulator for each of the eight storm/soil/slope scenarios, in which each emulator contained four random forests (one for each combination of cell type and target variable).

With cell type, target variable, and scenario held constant for each random forest, the input data consisted only of information regarding the spatial pattern of (im)permeable areas. While the spatial patterns are two-dimensional, the random forest model is a point-scale operator, meaning that the spatial pattern information had to be represented as a vector of “features” that described the spatial context of each point (cell;

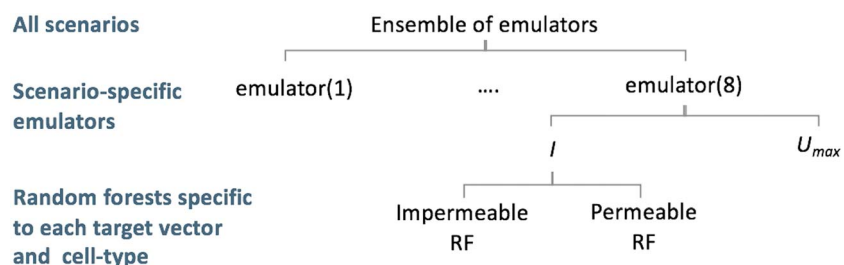


Figure 4. Schematic outlining the hierarchy of random forests that compose the “ensemble” of emulator models. RF = random forest.

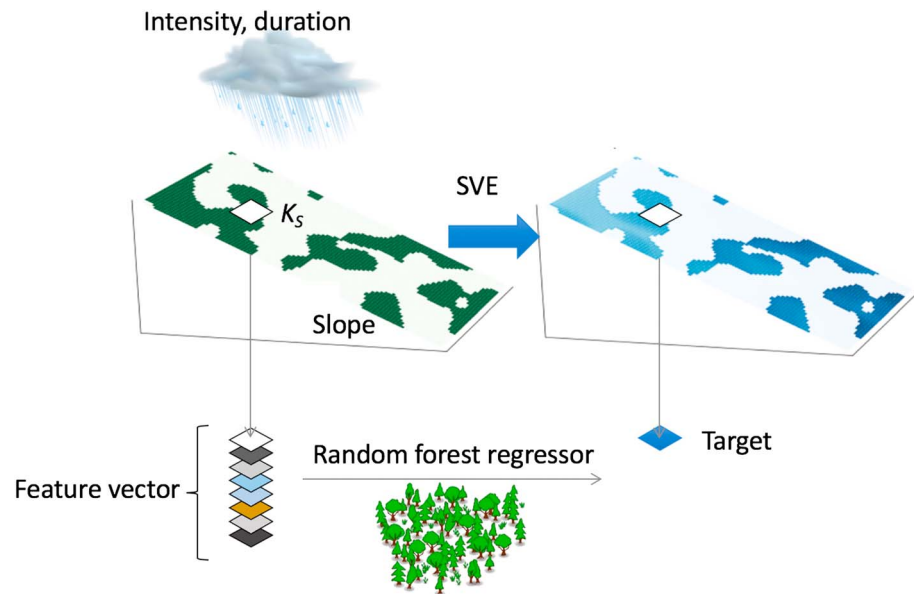


Figure 5. The hillslope on the left represents the SVE model domain, including spatial patterns, storm characteristics, soil parameters, and hillslope gradient. The hillslope on the right shows an SVE model prediction of infiltration depth, representing the target variable. Each point in the SVE model domain is transformed into a 1-D vector of features that represent the surrounding neighborhood. The random forest independently operates on each point to predict the outcome. SVE = Saint Venant equation.

see Figure 5). The features needed to provide enough spatial information that point-scale predictions of the target variables (I or U_{\max}) would reproduce the spatial properties of the SVE output when the cells were reassembled into a two-dimensional grid.

To identify potential features, we generated a list of spatial properties that we expected would influence infiltration and flow velocities at a given cell location: the length of the adjacent upslope (im)permeable area, the distance to the no-flux boundary at the divide, and the distances to the nearest cell of the opposite type in the upslope, lateral, and downslope directions. We found that these features were substantially independent of each other (see Pearson's correlation coefficients, shown in supporting information Table S2) and that each

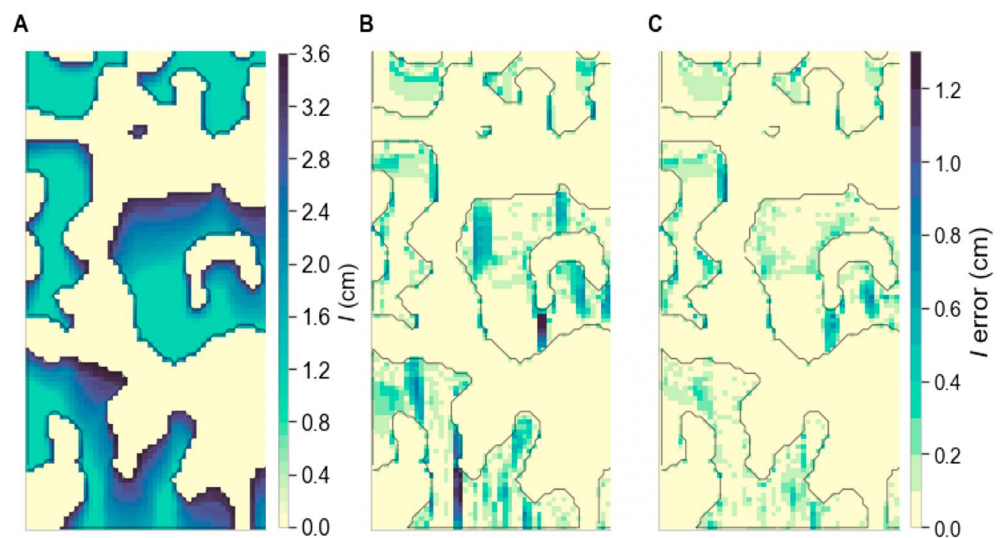


Figure 6. For a sample SVE simulated infiltration field (a), a side-by-side comparison of the errors for emulators fit to the core (b) and best fit (c) feature set. The simulation parameters are $p = 5$ cm/hr, $K_s = 8$ cm/hr, $S_o = 2\%$, $\phi_V = 0.4$, and $\sigma = 3$. SVE = Saint Venant equation.

Table 2
Features Used to Fit the Random Forests

Feature	Description
Permeable area features	
L_{UI}	Length of the nearest upslope impermeable area
d_{UI}	Distance to the nearest upslope impermeable cell
d_{DI}	Distance to the nearest downslope impermeable cell
d_{LI}	Across-slope (lateral) distance to the nearest impermeable cell
Impermeable area features	
L_{UP}	Length of the nearest upslope permeable area
d_{UP}	Distance to the nearest upslope permeable cell
d_{DP}	Distance to the nearest downslope permeable cell
d_{LP}	Across-slope (lateral) distance to the nearest permeable cell
Common features	
L_{div}	Distance to the divide
ϕ_P	Hillslope-mean permeable fraction
Feature parameters	
ζ	Standard deviation of the Gaussian kernel used in feature smoothing. $\zeta = 0$ indicates the original core features.
<p><i>Note.</i> For the best fit model, Gaussian smoothing was applied to all of the features, with the exception of ϕ_P and the distance to the divide. Both the smoothed and original versions were included as features.</p>	

of them was necessary to make reasonable predictions with a random forest model. We therefore designated these as the “core” features (example maps of which are provided in supporting information Figure S7).

The core features represent the influences of along- and across-slope flows only. Predictions made with emulators using only the core features contained linear spatial artifacts, due to their inability to represent the two-dimensional nature of the shallow water flow. An illustration of such artifacts is provided in Figure 6.

To remove these artifacts from the emulator predictions, we included additional features that incorporated information about the two-dimensional neighborhood of each cell in the prediction set. This was achieved by smoothing the core features with a Gaussian filter (see supporting information Figure S8 for visual examples of feature smoothing). Smoothing was applied to all features except ϕ_P and the distance to the divide L_{div} . We explored the sensitivity of the model performance to the degree of smoothing by varying the standard deviation ζ of the Gaussian kernel, where $\zeta = 0$ denotes the core, presmoothed features.

Feature smoothing generates strongly correlated features, which can impact model interpretability and generalizability. To avoid issues of model interpretability, we separately specified two versions of the emulator models: (i) a version that used only the core features and (ii) a “best fit” version that included feature smoothing. The spatial features ultimately used for prediction are defined in Table 2, where both the original and smoothed features were included in the best fit feature set. The smoothing length scales ζ needed to improve the model predictions and to correct for spatial artifacts were selected in the model tuning stage, detailed in the next section.

The random forest algorithm has a number of “hyperparameters” that control the nature and number of the regression trees in the forest (Pedregosa et al., 2011). Exploratory tests indicated minimal sensitivity of the predictions to most hyperparameters, with the exception of those limiting the size of the component regression trees. Of these, we elected to tune the maximum depth of the regression trees, with the dual considerations of (i) minimizing overfitting and (ii) limiting storage/memory requirements.

2.4. Emulator Model Tuning

For each target variable, we assessed the fidelity with which the emulator reproduced the within-hillslope spatial patterns and the hillslope-aggregate errors. The former was measured as the normalized root-mean-square error (NRMSE) between the SVE and emulator predictions:

$$\text{NRMSE} = \frac{1}{\chi_{\max} - \chi_{\min}} \sqrt{\frac{1}{N_{\text{cell}}} \sum_{N_{\text{cell}}} (\chi - \chi_{RF})^2} \quad (6)$$

where χ is the SVE model prediction (I or U_{\max}), χ_{RF} is the emulator prediction, $(\chi_{\max} - \chi_{\min})$ is the range of values predicted by the SVE model across the hillslope, and summation over N_{cell} is over all of the points in the hillslope domain.

To characterize the hillslope-aggregate errors, we examined the infiltration fraction IF and hillslope-mean maximum velocity $\langle U_{\max} \rangle$ errors:

$$\epsilon_{IF} = IF_{RF} - IF_{SVE}$$

$$\epsilon_{\langle U_{\max} \rangle} = \langle U_{\max} \rangle_{RF} - \langle U_{\max} \rangle_{SVE}$$

2.4.1. Cross Validation

Cross validation was used to refine the random forest hyperparameters and length scales of feature smoothing. Standard random forest implementations estimate errors internally and protect against overfitting by using the out-of-bag samples (the subsets of the data not used to grow the trees) to calculate the goodness of fit (Breiman, 2001). These internal errors are estimated on a cell-by-cell basis for a subset of the cells on any given hillslope. Since the out-of-bag samples are selected randomly from the highly spatially correlated I and U_{\max} fields, these internal errors risk being substantially biased due to autocorrelation between training cells and out-of-bag samples. This issue is likely to be particularly problematic for large patch length scales σ . Therefore, to assess the simulation-level errors, we subdivided simulations into training and validation subsets such that the training and validation sets were always drawn from different SVE simulations. Emulator model specifications were then selected to minimize the mean errors of the validation sets (see supporting information Text S2 for details).

K-fold cross validation was used to identify (i) the smoothing length scales ζ and (ii) the maximum depth of the regression trees. The simulations were split into five train/validation sets according to pattern morphology, where each validation set corresponded to a different value of σ . For each cross-validation fold, four of these sets were used to train the random forests, and the errors were assessed using prediction made on the fifth validation set. The length scales of feature smoothing and the random forest maximum depth were selected to minimize the mean validation errors within the tested parameters, using the metrics defined in section 2.4 averaged over all of the validation sets. Further description of the cross-validation methods are included in supporting information Text S2. Based on the cross-validation results, we selected a maximum depth = 10 for the core features and a best fit feature set with smoothing lengths of $\zeta = 0, 1, 2$ and maximum depth = 11.

As a final sensitivity test, Monte Carlo (random sampling) cross validation was used to assess the sensitivity of the errors to the number of training patterns (see supporting information Text S2). The emulator performance only marginally improved past 30 training patterns, and thus the 45 patterns used for training here provided a sufficient training space of patterns (see supporting information Figure S3).

2.5. Model Assessment

To assess the emulator performance on the training simulations, we computed the validation errors using the same k-fold cross-validation approach as used for model tuning. The errors for each validation fold (value of σ) were assessed with the emulator model fit to the remainder of the simulation data, and the final error estimated by averaging over the validation folds. The validation errors were computed for each of the four error metrics in section 2.4 and for the core and best fit feature sets.

Given the correlated features in the training data (a consequence of the common Gaussian smoothing operator), the emulator models risk overfitting to the training patterns, which would result in poor generalization to different spatial correlation structures (Matsuki et al., 2016). To test for any effects of this nature, we evaluated the emulator models performance using the anisotropic and suburban test patterns, which have different spatial correlation structures than the training patterns.

2.6. Model Interpretation

The random forest feature importances were used to identify which spatial properties drove the hydrological outcomes and if the most important properties varied with storm and landscape characteristics. We calculated the “drop-column importance” of each of the core features (Parr et al., 2018). The drop-column

Table 3
Spatial Metrics Computed for Each of the 1,000 Sampled Patterns

Feature	Description
ϕ_P	Permeable fraction
L_P	Mean along-slope length of the permeable areas
W_P	Mean across-slope width of the permeable areas
$\log(L_P/W_P)$	A measure of permeable area anisotropy and orientation
L_I	Mean along-slope length of the impermeable areas
W_I	Mean across-slope width of the impermeable areas
$\log(L_I/W_I)$	A measure of impermeable area anisotropy and orientation
A_{DC}	Directly connected impermeable area (the mean along-slope length of impermeable areas directly connected to the downslope boundary)
λ_P	Pattern wavelength
θ_P	Pattern direction
P/A	Mean permeable-area perimeter to area ratio

Note. All metrics denote averages over the entire hillslope domain, and $\langle \rangle$ notation is omitted for simplicity. Note that L_I is equivalent to the Flowlength index in Mayor et al. (2008).

importance of a feature is computed by comparing the error in a trained random forest model to a retrained version of the model from which the feature has been omitted. The feature's importance is the difference between the baseline and the retrained model. This offers a direct—but computationally expensive in the case of models with many predictor features—route to computing feature importance. Here, with six core features for each cell type, the computational costs were small.

2.7. Case Study: Predicting Hillslope-Scale Behaviors With Simple Spatial Metrics

As a case study to illustrate a potential application of the emulator model, we used it to explore the question of whether simple spatial metrics that describe the pattern of (im)permeable surfaces on a hillslope provide a robust basis with which to predict how that hillslope will function hydrologically. Specifically, we attempted to predict hillslope-scale infiltration fraction IF with such metrics.

We used the emulator model to predict IF for 1,000 spatial patterns with varying permeable fractions, patch length scales, and degrees of anisotropy, which we generated using the same approach as used to generate the anisotropic test set patterns (see section 2.2.2). These patterns were created by randomly sampling the values of σ_x , σ_y , ϕ_P from uniform distributions ($\phi_P \in [0.1, 0.9]$, $\sigma_x, \sigma_y \in [0, 10]$, $\sigma_x/\sigma_y \in [0.1, 10]$). Predicted

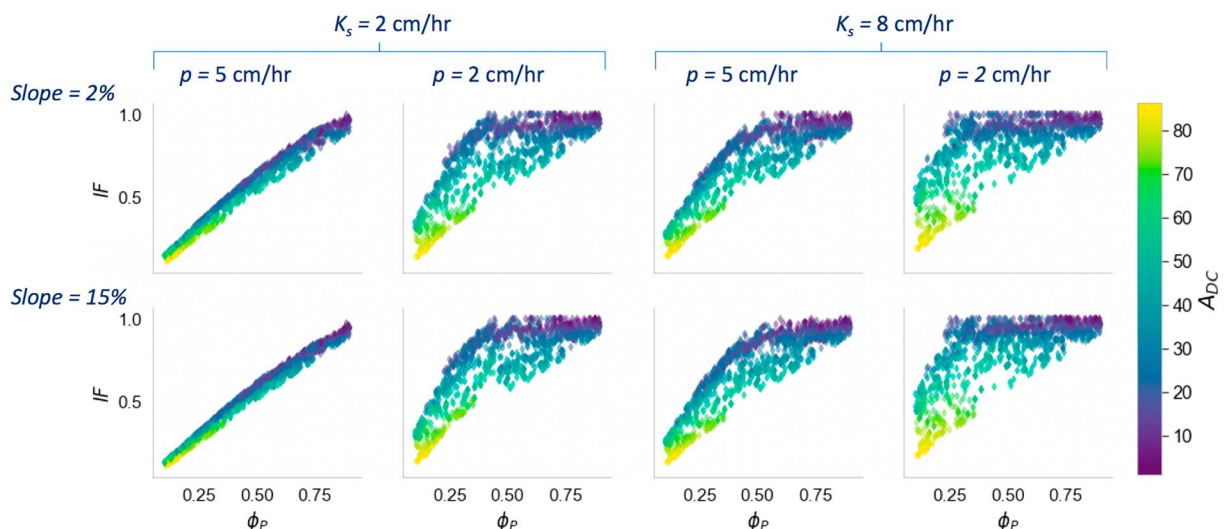


Figure 7. Scatter plots of emulator-predicted IF versus ϕ_P grouped by scenario, with marker color indicating A_{DC} . IF = infiltration fraction.

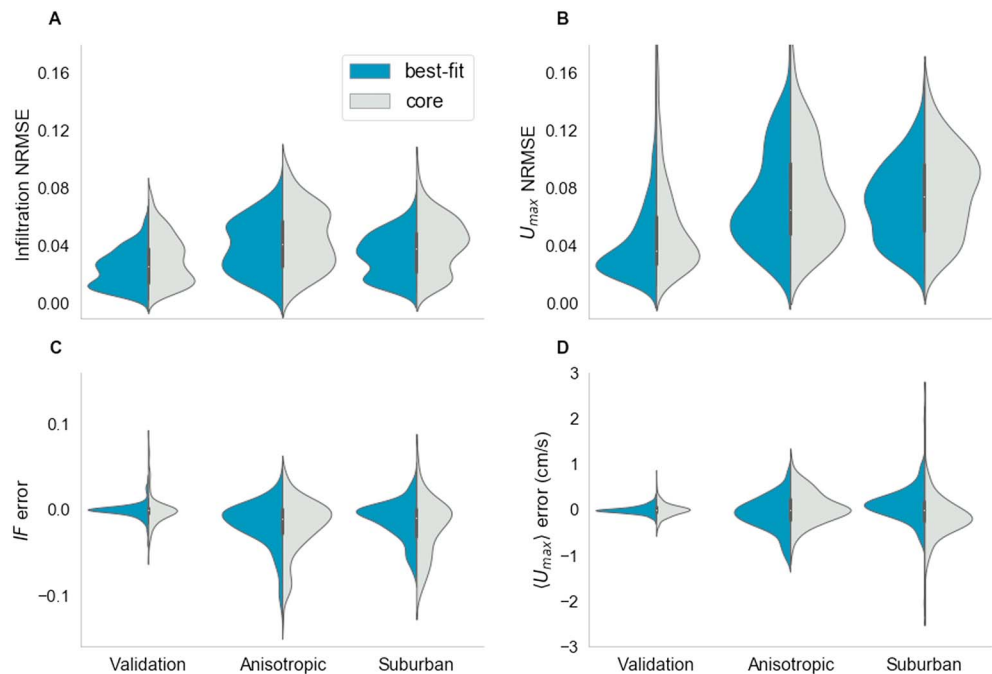


Figure 8. Emulator errors grouped by pattern set, with color indicating the feature set (core vs. best fit): (a) I NRMSE, (b) U_{\max} NRMSE, (c) IF errors and (d) $\langle U_{\max} \rangle$ errors. NRMSE = normalized root-mean-square error; IF = infiltration fraction.

across the eight scenarios in the emulator model, these 1,000 spatial patterns generated a total of 8,000 IF predictions.

For each pattern, we computed a number of summary, hillslope-scale spatial metrics, as listed in Table 3. The spatial metrics included the mean along-slope length and across-slope width of the (im)permeable areas, and the mean length to width ratios of the permeable areas as a measure of patch anisotropy and orientation. The directly connected impermeable area A_{DC} was computed as the mean along-slope length of impermeable areas directly connected to the downslope boundary. The pattern wavelength λ_p and direction θ_p were estimated using the Fourier windowing method of Penny et al. (2013).

We then undertook exploratory analyses to assess the potential for the metrics in Table 3 (independent variables) to predict the emulator-predicted IF (dependent variable). This analysis indicated that the permeable fraction ϕ_p and the directly connected impermeable area A_{DC} explained most of the variation in IF , as illustrated in Figure 7. We retained these features for further analysis, recognizing that these features are independent of each other, while substantially correlated to many of the other metrics in Table 3. These two hillslope-scale features can be interpreted in physical terms as follows: the permeable fraction of the hillslope ϕ_p measures the potential for the hillslope to generate runoff, while the directly connected impermeable area A_{DC} measures the fraction of the runoff which cannot infiltrate on the hillslope.

While the ϕ_p and A_{DC} features are independent of each other, they are substantially correlated to many of the other metrics in Table 3. For this reason, we retained only ϕ_p and A_{DC} for further analysis. We used an additional random forest to relate the emulator-predicted IF to ϕ_p and A_{DC} and assessed the quality of the results across the eight scenarios.

3. Results

3.1. Model Performance

The prediction errors, used to evaluate the model performance, are summarized in Figure 8 for all three pattern sets (isotropic, anisotropic, and suburban). In this figure, blue shading indicates the performance of the best fit model, and gray shading the performance of the core feature version. The I and U_{\max} NRMSE are shown in the upper panels, where the results can be interpreted as a proportional error. The hillslope-scale

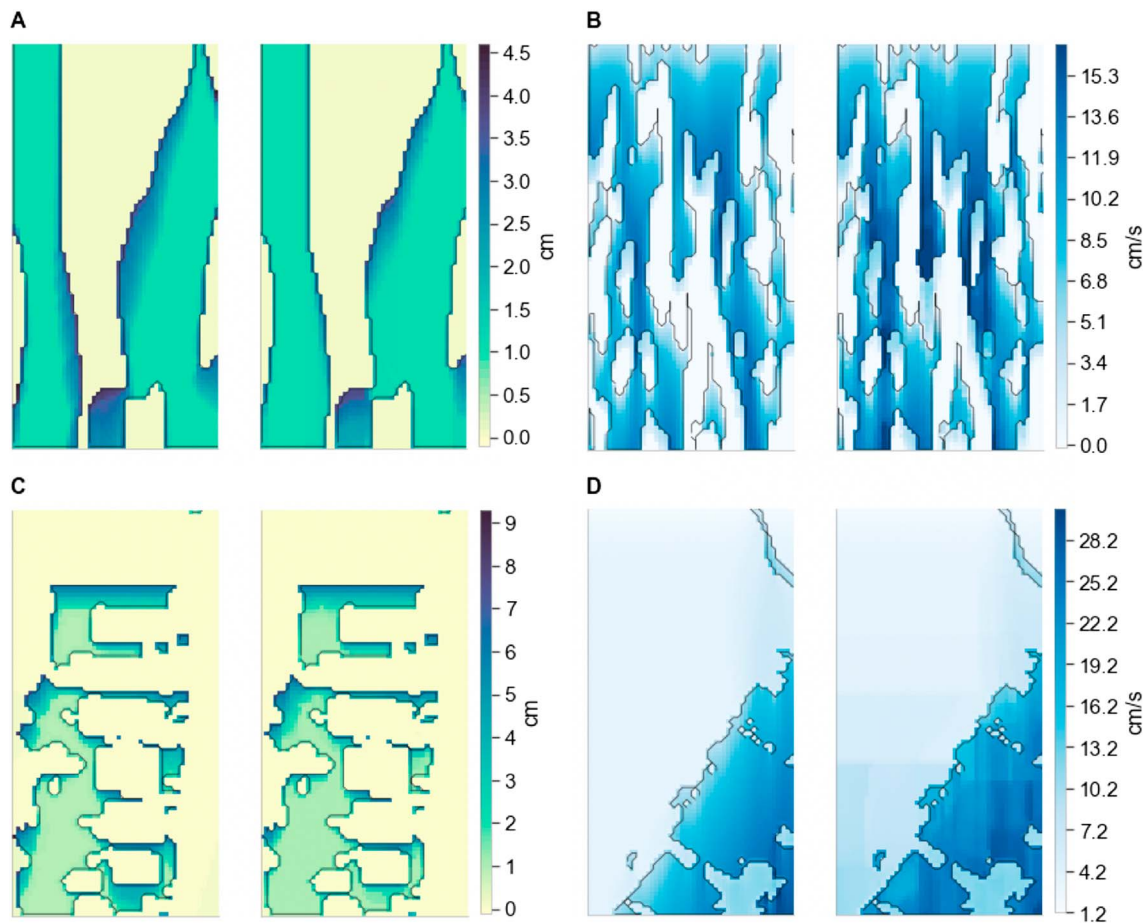


Figure 9. Visual performance of emulator output for the worst performing cases in the (a and b) anisotropic patterns and (c and d) suburban patterns. Separate patterns are shown for the infiltration fraction (a and c) and maximum velocities (b and d). For each pair of images, the left-hand side shows the SVE model output, and the right-hand side shows the emulator output. Details of the error and scenario used in each case are as follows: (a) IF error = -0.11 , $K_s = 2.0$ cm/hr, $p = 2.0$ cm/hr, $S_o = 2\%$; (b) $\langle U_{max} \rangle$ error = -1.1 cm/s, $K_s = 8.0$ cm/hr, $p = 2.0$ cm/hr, $S_o = 15\%$; (c) IF error = -0.07 , $K_s = 8.0$ cm/hr, $p = 2.0$ cm/hr, $S_o = 2\%$; and (d) $\langle U_{max} \rangle$ error = -2.0 cm/s, $K_s = 8.0$ cm/hr, $p = 2.0$ cm/hr, $S_o = 15\%$. SVE = Saint Venant equation; IF = infiltration fraction.

IF and $\langle U_{max} \rangle$ errors are shown in the lower panels, where errors are in absolute terms, and positive values indicate that the emulator predictions were larger than the SVE predictions.

For both the within-hillslope and hillslope-aggregate errors, the validation and test set errors are comparable. This suggests that the emulator models successfully generalized to new types of spatial patterns. The infiltration and U_{max} NRMSE were less than 12% and 16%, respectively, regardless of pattern configuration. The larger NRMSE for U_{max} reflect the normalization by very small velocities in some simulation instances and correspond to numerically small velocity errors. The hillslope-averaged $\langle U_{max} \rangle$ errors are less than 1 cm/s in most cases, while the impermeable-area U_{max} typically ranged from 5–30 cm/s.

The results indicate that the emulator models perform very well, with mean I and U_{max} NRMSE less than 2.3% and 3.3% for the best fit emulators tested on the isotropic patterns (validation set). As expected, the emulator performance is best for the best fit features and validation patterns, but the decline in performance when using the core features, or when tested on anisotropic or suburban patterns, is minimal (order 1% increase in error).

Supporting information Figures S9–S11 show variation in the model performance across the different scenarios (storm/soil/slope) for the isotropic, suburban, and anisotropic pattern sets. Although errors are always smallest for the $K_s = 2$, $p = 5$ cases (the case where both permeable and impermeable surfaces generate runoff, resulting in relatively homogeneous I and U_{max} fields), there is little systematic variation in model performance as a function of scenario. Similarly, the variation of model performance with the

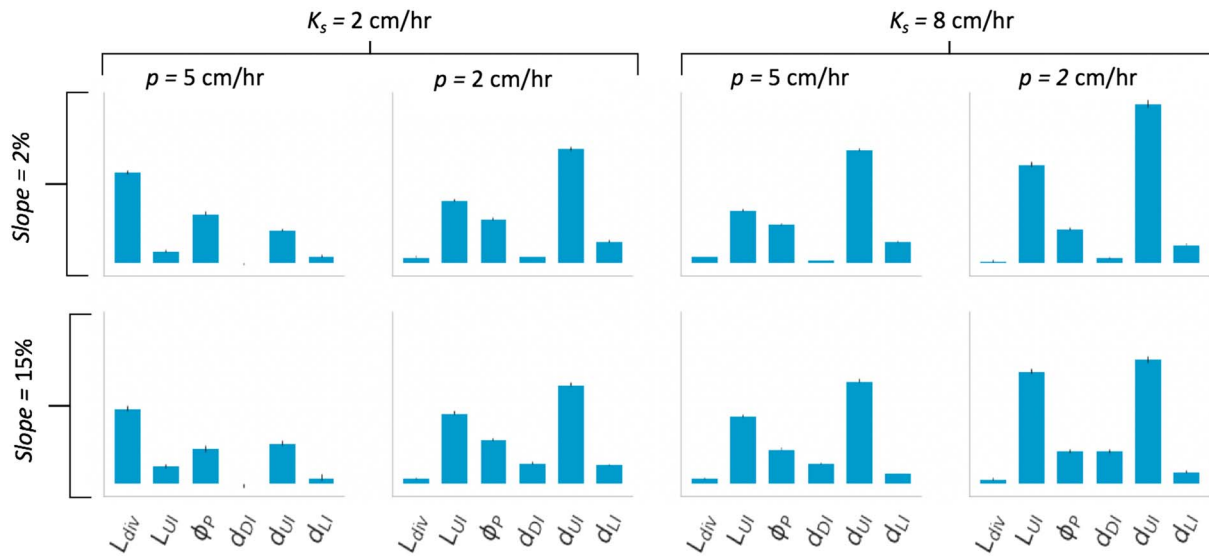


Figure 10. Permeable-area feature importances for I (impermeable areas are omitted). Feature importances are grouped by slope, p , and K_s . Note that there is no y axis, because all feature importances are scaled to sum to 1. Because feature importances can vary across all trees in the random forest, the results shown here are the average (when importances are computed independently for each tree), with the standard deviation shown as error bars.

characteristics of the spatial pattern was minimal (see supporting information Figure S12). Finally, visual assessment of model performance is provided for the worst performing cases in Figure 9, which compare emulator and SVE predictions for the anisotropic and suburban test sets. Emulator errors generally arise from underestimation of infiltration from runoff-run-on processes.

These errors/performance imperfections arise in the context of a 15,000-fold reduction in model runtime. The mean SVE model runtime was 13.6 hr/simulation. The emulator models needed less than 50 ms to predict I and U_{\max} for the same 100×50 -m domain.

3.2. Interpretation

The random forest feature importances, and how they vary across the scenarios, offer insight into which spatial properties of the (im)permeability pattern have the greatest influence on U_{\max} and I . These importances are shown, grouped by scenario, for the infiltration field I in Figure 10. In this figure, the impermeable area is excluded due to the minimal infiltration occurring in these areas.

The most important features controlling infiltration vary across the scenarios. For example, the distance to the nearest upslope impermeable area d_{UI} is the most important feature in most cases, followed by the length of the nearest upslope impermeable area L_{UI} . However, in the scenarios with $p = 5$ cm/hr and $K_s = 2$ cm/hr, the distance to the divide L_{div} is the dominant feature. We attribute this to the fact that, when $p = 5$ cm/hr and $K_s = 2$ cm/hr, the entire hillslope acts as a runoff source, and the spatial pattern of infiltration is determined by what happens to the ponded water after the rain stops. The distance to the divide is the primary control on the depth of ponded water at the end of the rain and therefore the most important factor influencing the cumulative infiltration depth at a given point. For the other scenarios, infiltration is more strongly controlled by run-on from the surrounding impermeable areas and thus by the distance to and strength of the nearest upslope sources (d_{UI} and L_{UI} , respectively). The feature importances for d_{DI} and d_{LI} are small but positive in most cases, which is consistent with visual inspection of the infiltration maps in Figure 3, where d_{DI} and d_{LI} are only relevant for permeable cells adjacent to impermeable cells. Finally, the sensitivity to hillslope gradient is small (the differences between the upper $S_o = 2\%$ and lower $S_o = 15\%$ rows are minor). We note, however, that hillslope gradient is likely to play an important role for predicting other hillslope metrics, for example, timing or duration of peak discharge, and is known to be a key factor for driving subsurface stormflow (Hopp & McDonnell, 2009).

Figure 11 displays the U_{\max} feature importances for permeable and impermeable areas. I and P subscripts are omitted in the x axis labels to represent both cell types: L_U is the length of the nearest upslope area of the opposite cell type, and d_U , d_D , and d_L are the upslope, downslope, and lateral distances to the nearest

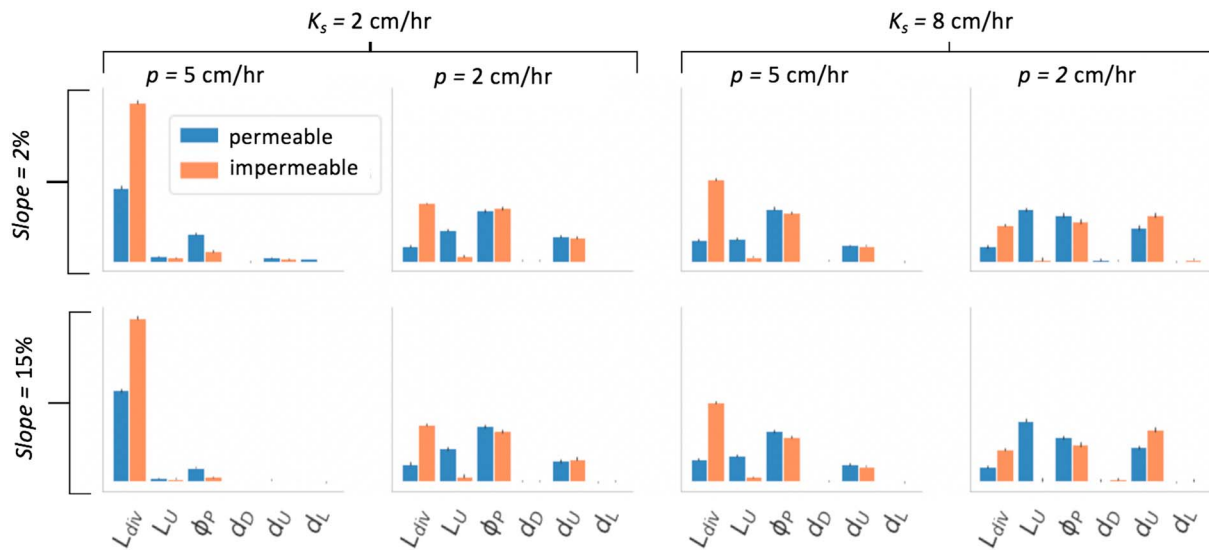


Figure 11. Feature importances for U_{\max} , for permeable (blue) and impermeable (orange) areas. Feature labels are abbreviated; for example, L_U refers to length of the upslope patch area of the opposite type (L_{UI} for impermeable areas, and L_{UP} for permeable areas).

cells of the opposite type. In all scenarios, L_{div} is a more important feature for impermeable areas than for permeable areas, and L_U is more important for permeable areas. This suggests that U_{\max} in permeable areas is more strongly influenced by the nearest upslope impermeable area, whereas U_{\max} in impermeable areas is more sensitive to the global source area.

Comparing the feature importances between Figures 10 and 11, L_{div} is a more important feature for U_{\max} in all scenarios. While d_{UI} is the most important feature for predicting I in most scenarios, d_{UI} and the analogous d_{UP} are relatively less important for U_{\max} . Differences in feature importances between U_{\max} and I are not surprising, given that U_{\max} is a snapshot of the overland flow at the end of the rain and I is a time-integrated field, influenced by overland flow during and after the rain ends. L_{div} is evidently a greater factor in how overland flow is distributed at the end of a storm, whereas d_{UI} and L_{UI} are important factors influencing where that water infiltrates or runs off after the storm ends.

3.3. Case Study: Predicting Hillslope-Scale Behaviors With Simple Spatial Metrics

The random forest regressions relating IF to the hillslope-scale spatial metrics ϕ_p and A_{DC} for each scenario showed excellent predictive skill. For all scenarios, IF predictions with $r^2 > 0.97$ and $\text{RMSE} < 3.5\%$ were achieved (when compared to the emulator predictions). If SVE simulations are used as a basis for comparison, the performance was $r^2 > 0.87$ and $\text{RMSE} < 5.6\%$ (see supporting information Table S3 and Figure S13), where the decrease in predictive skill reflects the dual sources of error in the emulator model and the subsequent $IF \sim \phi_p + A_{DC}$ random forest regression.

The most interesting result, however, is that the prediction of IF and its dependence on the hillslope-scale metrics is *not stable* across scenarios. This is illustrated in Figure 12, which shows the feature importances for the random forest regression of IF on A_{DC} and ϕ_p , sorted from left to right in order of increasing $K_s - p$ (see supporting information Table S3). Feature importances should be interpreted here as analogous to an effect size in a traditional linear regression, in that they measure the sensitivity of the errors to variation in the predictor variables.

The relative importance of ϕ_p and A_{DC} varies among the scenarios, as a function of (i) the volume of runoff generated on impermeable areas and (ii) the capacity of the permeable areas to intercept and absorb the runoff before it runs off the hillslope. In cases where $p > K_s$, runoff production is the main dynamic on the hillslope, and ϕ_p closely predicts the infiltration fraction. However, in cases where $K_s \ll p$, A_{DC} dominates because permeable areas infiltrate most runoff that runs onto them, and the only runoff that does not infiltrate is that which is produced on directly connected impermeable areas. In between these end cases, both dynamics are in play, leading to the intermediate cases seen in Figure 12.

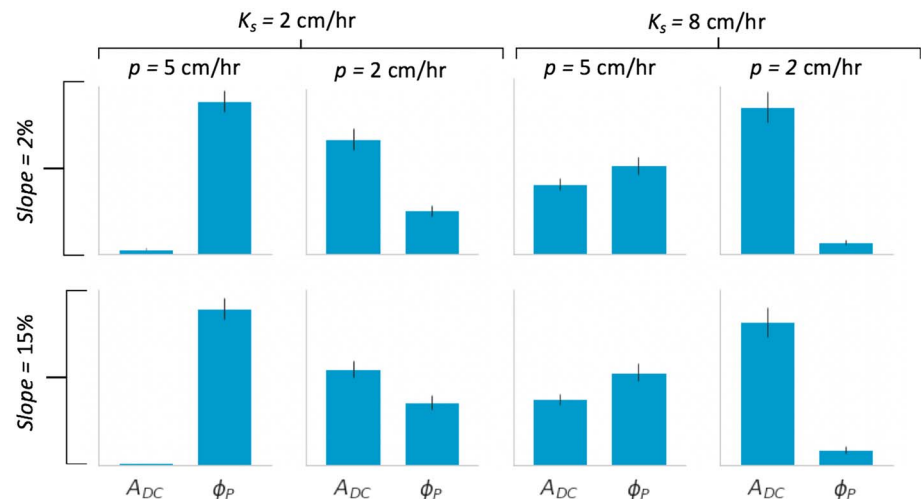


Figure 12. Drop-column feature importances for the random forest regression of IF on A_{DC} and ϕ_P . Error bars indicate the standard deviation of feature importances when independently computed for each tree in the forest. IF = infiltration fraction.

4. Discussion

4.1. Emulator Model Performance

The emulator model presented here reproduced the SVE results well. The emulator errors, on the order of 5%, are comparable to or smaller than those associated with both the parameterization and validation of hydrological models in natural environmental settings, suggesting that there is little to be lost (and much simplification to be gained) by replacing the SVE with an emulator model. We recognize that we did not fully optimize the emulator. However, our analyses showed limited sensitivity of the model performance to any of its parameters (supporting information Figures S1–S3). This suggests that it is unlikely for the high quality performance of the present model to substantially improve if a formal optimization were attempted. Given the very large number of ways in which spatial patterns can be disaggregated into features, true optimization of a potential emulator model would represent a major computational challenge, one which the results of the present model suggest may not be worth undertaking.

The model performance and error characterization provided here applies only to the spatial (i.e., 50×100 m) and temporal (i.e., individual storm) scales associated with the simulations. Over repeated simulations, as would be needed to reproduce longer-term climatologies or to run coupled plant population-hydrology models, the errors are likely to aggregate in nonlinear and hard-to-predict ways; longer-term simulations require independent error assessment. Upscaling through space may be less challenging in some cases; for example, in those scenarios where the distance to the divide is a small factor in predicting I and U_{\max} (e.g., $K_s > p$) the errors associated with arbitrarily extending the hillslope length would likely be small. However, upscaling also requires assessing the occurrence of concentrated flow paths (omitted in this model) and correctly imposing other watershed geomorphic phenomena (e.g., changing soil or slope gradients along the hillslope catena; Fraser et al., 2013).

Despite relying on the use of correlated predictive features (the smoothed features) to account for the two-dimensional nature of the flow and correct for linear artifacts produced when smoothing was omitted (as shown in Figure 6), the resulting emulators were highly generalizable to novel pattern types. Feature smoothing in fact improved the NRMSE results in 80% of the anisotropic and 95% of the suburban simulations (with comparable results for U_{\max}) relative to predictions made with the core features only. This suggests that the multicollinearity introduced by smoothing did not result in overfitting or loss of generality.

4.2. Case Study: Predicting Hillslope-Scale Behaviors With Simple Spatial Metrics

The case study explored the degree to which simple spatial metrics could be used to predict hydrological outcomes. Like other studies of connectivity metrics (e.g., Mayor et al., 2008), we found that the explored metrics were indeed related to runoff behavior, as measured in this case by the infiltration fraction. By eval-

uating two metrics together and exploring how the relationships to infiltration fraction varied with storm and hillslope characteristics, however, we were able to advance on previous observations that the predictive skill of specific metrics varied with storm intensity. For instance, Mayor et al. (2008) found that their proposed “Flowlength” metric, which measures the accumulated length of potential runoff pathways defined on a slope with varying vegetation and microtopography characteristics, predicted runoff well under moderate rainfall conditions but lost predictive power as rainfall intensity decreased. Further, Turnbull and Wainwright (2019) found that Flowlength was more strongly related to functional connectivity (based on modeled flow paths) under moderate rather than high-intensity rainfall conditions. Finally, the importance of “thresholds” of rainfall intensity for initializing connection in infiltration excess dominated landscapes is highlighted in the conceptual and mathematical framework presented by Ali et al. (2018).

The results presented in these previous studies are comparable with those in our emulation study, which suggest that directly connected impermeable area is a more important predictor of runoff under low rainfall intensities, vegetation fraction is a more important predictor under high rainfall intensities, and both are needed to make predictions for moderate cases. We note, as an aside, that Flowlength was highly correlated with the directly connected impermeable area in our case study but did not explain as much variation in infiltration fraction as the directly connected impermeable area. Taken together, these findings suggest that (i) more than one spatial or connectivity metric may be needed to describe hydrologic functions across a range of conditions and (ii) different metrics are likely to be associated with different realms of predictive power. At a minimum, these results demonstrate that caution should be exercised when using spatial metrics for hydrological prediction. Our results also raise the question of whether summarizing landscape complexity with spatial metrics is a viable pathway toward simplifying predictions in complex landscapes, given these limitations of predictive scope. While we have not fully unraveled these questions in the present study, our ability to emulate the SVE results for patchy landscapes provides opportunities to generalize prediction across many pattern realizations, potentially allowing these complexities to be unraveled.

4.3. Emulator Applications

In its current form, the emulator model is best suited to explore problems, like the one described in the previous case study, that depend on the spatial arrangement of permeable and impermeable surfaces. In dryland systems, this spatial arrangement is typically associated with the presence or absence of vegetation (Noy-Meir, 1979), due to the role of vegetation in protecting the soil surface, creating habitat for macrofauna, and suppressing the growth of biological soil crusts which reduce the permeability of bare soil sites (Belnap, 2006; Thompson et al., 2010). The emulator can thus be used to describe the ecohydrology of dryland ecosystems.

One possible application of the emulator model is the design of ecosystem restoration and rehabilitation, where understanding the effect of varying spatial patterns of plant organization is critical. Vegetation in drylands often relies on additional inputs of water derived from overland flow to support its growth (Ludwig et al., 2005, 2007; Tongway & Ludwig, 2001). Dryland revegetation efforts therefore need to support the formation of spatial patterns of vegetation where overland flow is generated and infiltration of this flow in vegetated sites is sufficient to meet plant water demands (Assouline et al., 2015). The emulator is well suited to assessing different potential planting patterns against plant water requirements and potentially also against erosion risks posed by high flow velocities.

Over decadal time scales, dryland ecosystems evolve through space, responding to different spatial patterns in resource availability (e.g., soil water) and mortality (e.g., water stress, herbivory, or biomass harvesting; Deblauwe et al., 2011, 2012; Penny et al., 2013; Rietkerk et al., 2000). To date, efforts to model such evolution have relied on patch dynamics models (e.g., Kéfi et al., 2007; Reynolds et al., 1997) and on phenomenological models which do not resolve storm-scale overland flow processes (Guttal & Jayaprakash, 2007; Rietkerk et al., 2002). These efforts have been limited by the computational demands associated with spatially representing water movement on storm scales (Paschalis et al., 2016; Thompson et al., 2011), which make simulation of the many hundreds to thousands of storms relevant to long-term ecosystem spatial evolution impossible. The tremendous computational acceleration offered by the emulator renders this problem tractable for the first time. Model diagnostic exercises that simulate how vegetation spatial organization changes as a function of storm characteristics would be an obvious initial application. Time series of storms, however, could also be simulated coarsely by classifying storms into a finite set of intensities and durations for which random forests could be trained.

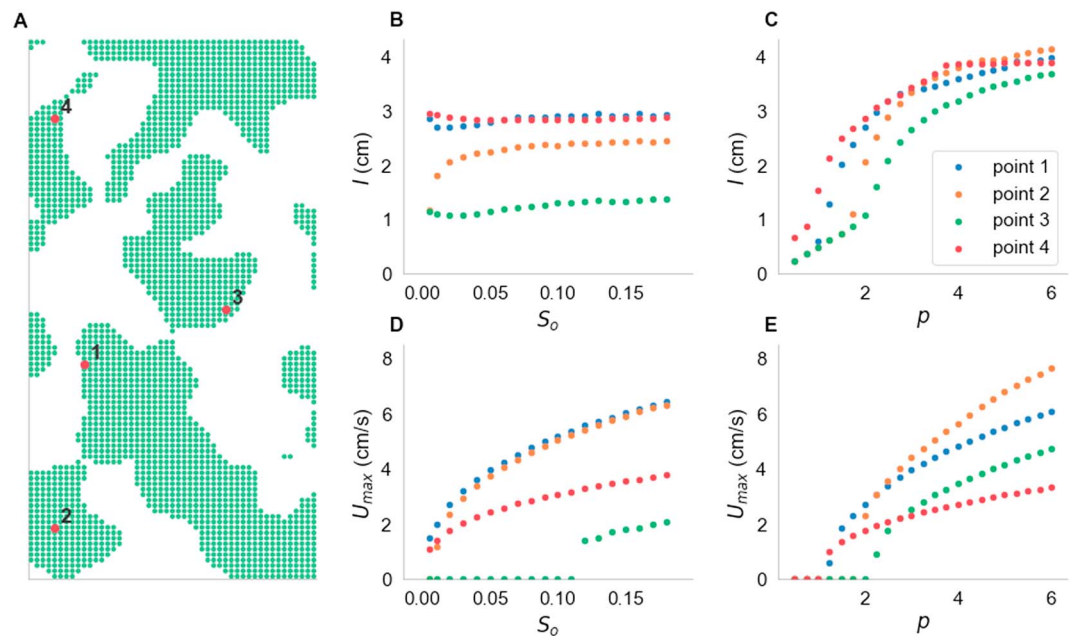


Figure 13. Potential to linearly interpolate pixel-scale cumulative infiltration or peak velocity across varying storm intensities and hillslope gradients, as illustrated for four distinct, vegetated points on the hillslope shown in (a). (b and c) Predictions of I for variations in S_0 (with $p = 4$ cm/hr) and p (with $S_0 = 2\%$). (d and e) Predictions of U_{\max} for the same cases.

Other applications for the emulator can be imagined where representative storm and landscape types are classified into a finite range of scenarios upon which the random forests are trained, within which the implications of different landscape patterns could be tested. Examples might include testing the sensitivity of stormwater runoff generation to different development configurations and land use planning scenarios in a city, covering a finite range of design storms and slopes. Applications of this nature require retraining of the random forests, rather than direct application of the scenarios tested above. In bespoke applications, it is likely that the emulator model would be most useful where the scenarios were selected based on end-user needs. Although this does not completely avoid use of the SVE, it does allow considerable speedup relative to simulation of multiple spatial scenarios and potentially a useful division of labor between modelers (who might run the training simulations) and ecologists, managers, or planners (who might use the trained emulator model). However, the limitations posed by needing to train multiple scenarios provoke the obvious question of whether the emulator can be further generalized.

To explore the potential for generalization in a preliminary way, we ran SVE simulations in which we varied hillslope gradient or storm intensity while holding the spatial pattern and other properties constant. We then assessed the variations in I and U_{\max} at randomly selected pixel locations with varying slope or storm intensity. An example of such variations is provided in Figure 13. For all points in the domain, we then asked how much error would be introduced by linear interpolation between different slopes and rainfall intensities. We replaced the modeled I or U_{\max} with interpolation from the surrounding S_0 or p values and examined how this error depended on the step size between the interpolated points. We computed the error as the root-mean-square error of all points in the domain, normalized by the mean of the nonzero values (NRMSE). As shown in Figure 14, the mean I NRMSE (of all points on a given hillslope) is less than 5% for $\Delta S_0 \leq 0.08$ and $\Delta p \leq 1.5$ cm/hr, and the mean U_{\max} NRMSE are less than 5% for $\Delta S_0 \leq 0.05$ and $\Delta p \leq 1.5$ cm/hr. This suggests that interpolation is a feasible approach to relate I and U_{\max} fields produced for different scenarios to each other. A path toward generalizing the emulator would therefore consist of training random forests for scenarios covering factorial combinations of SVE parameters, with an interpolation step to make predictions for arbitrary scenarios. We note that there are several outstanding issues with this approach that need to be resolved, for example, selecting an appropriate multivariate interpolation method. Similarly, there is likely some scope to optimize the parameter grid to minimize interpolation error across scenarios, subject to the computational and memory constraints associated with the training and storing of many random forests—reflecting, for example, our observation (data not shown) that the

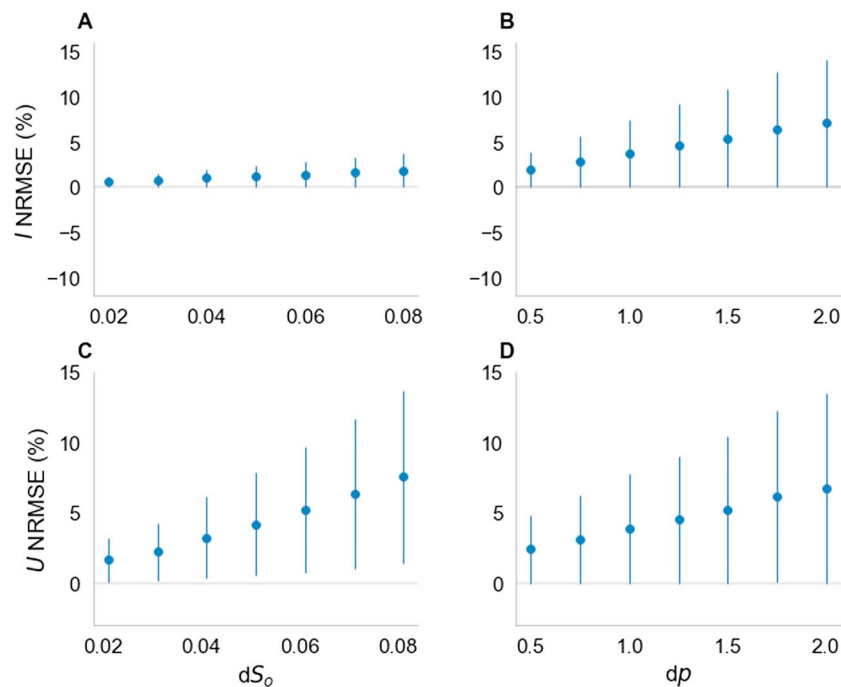


Figure 14. Sensitivity of I and U_{\max} interpolation error to varying p and S_0 interpolation step size. (a and b) The NRMSE of I when interpolated across hillslope gradients S_0 (a) and rainfall intensities p (b); (c and d) the NRMSE of the predicted U_{\max} for the same interpolation cases. The x axis shows the interpolation step size. Dots show the mean errors for all 5,000 points in Figure 13a, and error bars the standard deviation. NRMSE = normalized root-mean-square error.

interpolation error was lowest for high rainfall intensities and slopes. We have left the resolution of these questions and such generalization as a next step.

5. Conclusions

Emulation of the SVEs with a random forest regression offers a rapid, accurate, and powerful way to assess hydrological function for fixed combinations of landscape and storm properties across arbitrary spatial distributions of (im)permeable surfaces. There are, of course, numerous opportunities to advance on this work. For example, the framework presented here would benefit from straightforward extension such as broadening the range of soil, storm, and hillslope scenarios addressed by the ensemble emulator. Preliminary analysis suggests that meaningful interpolation *between* scenarios is possible, given a sufficiently rich data set. More substantial elaborations, such as incorporating surface microtopography and its spatial correlation with (im)permeable surface areas in the emulation framework, are also feasible extensions of the present approach. Overall, the excellent performance of the emulator for the SVE suggests that machine learning and emulation models provide a viable approach to making hydrological predictions on patchy landscapes with varying permeability and should be considered as an alternative, or aid, to general predictors of hydrological function.

References

- Alberti, M., Booth, D., Hill, K., Coburn, B., Avolio, C., Stefan, C., & Spirandelli, D. (2007). The impact of urban patterns on aquatic ecosystems: An empirical analysis in Puget lowland sub-basins. *Landscape and Urban Planning*, 80(4), 345–361. <https://doi.org/10.1016/j.landurbplan.2006.08.001>
- Ali, G., Oswald, C., Spence, C., & Wellen, C. (2018). The T-TEL method for assessing water, sediment, and chemical connectivity. *Water Resources Research*, 54, 634–662. <https://doi.org/10.1002/2017WR020707>
- Alley, W., & Veenhuis, J. (1983). Effective impervious area in urban runoff modeling. *Journal of Hydraulic Engineering*, 109(2), 313–319. [https://doi.org/10.1061/\(ASCE\)0733-9429\(1983\)109:2\(313\)](https://doi.org/10.1061/(ASCE)0733-9429(1983)109:2(313))
- Arnold, C., & Gibbons, J. (1996). Impervious surface coverage: The emergence of a key environmental indicator. *Journal of the American Planning Association*, 62(2), 243–258. <https://doi.org/10.1080/01944369608975688>
- Assouline, S. (2004). Rainfall-induced soil surface sealing. *Vadose Zone Journal*, 3(2), 570–591. <https://doi.org/10.2136/vzj2004.0570>

Acknowledgments

O. C. and S. E. T. acknowledge funding from NSF EAR-BSF1632494. A. S. acknowledges funding from NSF Engineering Research Center for ReInventing the Nation's Urban Water Infrastructure (ReNUWIt). We would also like to thank Scott F. Bradford and Nikolaos D. Katopodes for providing the code for the SVE solver, as described in Bradford and Katopodes (1999). The source code for the SVE model and the emulator feature generation code are hosted openly on GitHub (<https://github.com/octavia-crompton/SVE-R>). Code for the implementation of the random forest regressions is not provided, as we used the Python library scikit-learn with minimal modification (Pedregosa et al., 2011). The SVE solver is in Fortran, and Python wrapper scripts are provided to interface with Fortran. Jupyter notebooks are provided to visualize the results for selected examples. All data used in this study are publicly available: the landcover data set for Sonoma County is available for download online (<http://sonomavegmap.org/data-downloads/>).

- Assouline, S., Thompson, S., Chen, L., Svoray, T., Sela, S., & Katul, G. (2015). The dual role of soil crusts in desertification. *Journal of Geophysical Research: Biogeosciences*, 120, 2108–2119. <https://doi.org/10.1002/2015JG003185>
- Audsley, E., Pearn, K. R., Harrison, P., & Berry, P. (2008). The impact of future socio-economic and climate changes on agricultural land use and the wider environment in East Anglia and North West England using a metamodel system. *Climatic Change*, 90(1-2), 57–88. <https://doi.org/10.1007/s10584-008-9450-9>
- Belnap, J. (2006). The potential roles of biological soil crusts in dryland hydrologic cycles. *Hydrological Processes*, 20(15), 3159–3178.
- Bhaskar, A. S., Welty, C., Maxwell, R. M., & Miller, A. J. (2015). Untangling the effects of urban development on subsurface storage in Baltimore. *Water Resources Research*, 51, 1158–1181. <https://doi.org/10.1002/2014WR016039>
- Bhattacharjya, R. K., & Datta, B. (2005). Optimal management of coastal aquifers using linked simulation optimization approach. *Water Resources Management*, 19, 295–320. <https://doi.org/10.1007/s11269-005-3180-9>
- Booth, D. B., & Jackson, C. R. (1997). Urbanization of aquatic systems: Degradation thresholds, stormwater detection, and the limits of mitigation. *JAWRA Journal of the American Water Resources Association*, 33(5), 1077–1090. <https://doi.org/10.1111/j.1752-1688.1997.tb04126.x>
- Børgesen, C. D., Djurhuus, J., & Kyllingsbæk, A. (2001). Estimating the effect of legislation on nitrogen leaching by upscaling field simulations. *Ecological Modelling*, 136(1), 31–48. [https://doi.org/10.1016/S0304-3800\(00\)00386-0](https://doi.org/10.1016/S0304-3800(00)00386-0)
- Bracken, L. J., & Croke, J. (2007). The concept of hydrological connectivity and its contribution to understanding runoff-dominated geomorphic systems. *Hydrological Processes*, 21(13), 1749–1763. <https://doi.org/10.1002/hyp.6313>
- Bracken, L., Wainwright, J., Ali, G., Tetzlaff, D., Smith, M., Reaney, S., & Roy, A. (2013). Concepts of hydrological connectivity: Research approaches, pathways and future agendas. *Earth-Science Reviews*, 119, 17–34. <https://doi.org/10.1016/j.earscirev.2013.02.001>
- Bradford, S. F., & Katopodes, N. D. (1999). Hydrodynamics of turbid underflows. I: Formulation and numerical analysis. *Journal of Hydraulic Engineering*, 125(10), 1006–1015. [https://doi.org/10.1061/\(ASCE\)0733-9429\(1999\)125:10\(1006\)](https://doi.org/10.1061/(ASCE)0733-9429(1999)125:10(1006))
- Breiman, L. (2001). Random forests. *Machine Learning*, 45(1), 5–32. <https://doi.org/10.1023/A:1010933404324>
- Broad, D. R., Dandy, G. C., & Maier, H. R. (2005). Water distribution system optimization using metamodels. *Journal of Water Resources Planning and Management*, 131(3), 172–180. <https://doi.org/10.1016/j.envsoft.2014.11.015>
- Brutsaert, W. (2005). *Hydrology: An introduction*. Cambridge: Cambridge University Press.
- Castelletti, A., Galelli, S., Ratto, M., Soncini-Sessa, R., & Young, P. C. (2012). A general framework for dynamic emulation modelling in environmental problems. *Environmental Modelling & Software*, 34, 5–18. <https://doi.org/10.1016/j.envsoft.2012.01.002>
- Castelletti, A., Pianosi, F., Soncini-Sessa, R., & Antenucci, J. (2010). A multiobjective response surface approach for improved water quality planning in lakes and reservoirs. *Water Resources Research*, 46, W06502. <https://doi.org/10.1029/2009WR008389>
- Celia, M. A., Bouloutas, E. T., & Zarba, R. L. (1990). A general mass-conservative numerical solution for the unsaturated flow equation. *Water Resources Research*, 26(7), 1483–1496. <https://doi.org/10.1029/WR026i007p01483>
- Deblauwe, V., Couteron, P., Bogaert, J., & Barbier, N. (2012). Determinants and dynamics of banded vegetation pattern migration in arid climates. *Ecological Monographs*, 82(1), 3–21.
- Deblauwe, V., Couteron, P., Lejeune, O., Bogaert, J., & Barbier, N. (2011). Environmental modulation of self-organized periodic vegetation patterns in Sudan. *Ecography*, 34(6), 990–1001.
- Descroix, L., Viramontes, D., Estrada, J., Barrios, J.-L. G., & Asseline, J. (2007). Investigating the spatial and temporal boundaries of Hortonian and Hewlettian runoff in Northern Mexico. *Journal of Hydrology*, 346(3-4), 144–158. <https://doi.org/10.1016/j.jhydrol.2007.09.009>
- Farthing, M. W., & Ogden, F. L. (2017). Numerical solution of Richards equation: A review of advances and challenges. *Soil Science Society of America Journal*, 81, 1257. <https://doi.org/10.2136/sssaj2017.02.0058>
- Fletcher, T. D., Andrieu, H., & Hamel, P. (2013). Understanding, management and modelling of urban hydrology and its consequences for receiving waters: A state of the art. *Advances in Water Resources*, 51, 261–279. <https://doi.org/10.1016/j.advwatres.2012.09.001>
- Fraser, C., McIntyre, N., Jackson, B., & Wheeler, H. (2013). Upscaling hydrological processes and land management change impacts using a metamodeling procedure. *Water Resources Research*, 49, 5817–5833. <https://doi.org/10.1002/wrcr.20432>
- Fry, T. J., & Maxwell, R. M. (2017). Evaluation of distributed BMPs in an urban watershed—High resolution modeling for stormwater management. *Hydrological Processes*, 31(15), 2700–2712. <https://doi.org/10.1002/hyp.11177>
- Garcet, J. P., Ordonez, A., Roosen, J., & Vanclooster, M. (2006). Metamodeling: Theory, concepts and application to nitrate leaching modelling. *Ecological Modelling*, 193(3-4), 629–644. <https://doi.org/10.1016/j.ecolmodel.2005.08.045>
- García-Alba, J., Bárcena, J. F., Ugarteburu, C., & García, A. (2018). Artificial neural networks as emulators of process-based models to analyze bathing water quality in estuaries. *Water Research*, 1(150), 283–295. <https://doi.org/10.1016/j.watres.2018.11.063>
- Giraldez, J. V., & Woolhiser, D. A. (1996). Analytical integration of the kinematic equation for runoff on a plane under constant rainfall rate and Smith and Parlange infiltration. *Water Resources Research*, 32, 3385–3389. <https://doi.org/10.1029/96WR02106>
- Govers, G. (1992). Relationship between discharge, velocity and flow area for rills eroding loose, non-layered materials. *Earth Surface Processes and Landforms*, 17(5), 515–528. <https://doi.org/10.1002/esp.3290170510>
- Guttal, V., & Jayaprakash, C. (2007). Self-organization and productivity in semi-arid ecosystems: Implications of seasonality in rainfall. *Journal of Theoretical Biology*, 248(3), 490–500.
- Hoffman, O., Yizhaq, H., & Boeken, B. (2017). Shifts in landscape ecohydrological structural–functional relationship driven by experimental manipulations and ecological interactions. *Ecohydrology*, 10(3), e1806. <https://doi.org/10.1002/eco.1806>
- Hopp, L., & McDonnell, J. (2009). Connectivity at the hillslope scale: Identifying interactions between storm size, bedrock permeability, slope angle and soil depth. *Journal of Hydrology*, 376(3-4), 378–391.
- Horton, R. E. (1933). The role of infiltration in the hydrologic cycle. *Transactions, American Geophysical Union*, 14(1), 446. <https://doi.org/10.1029/TR014i001p00446>
- Jones, E., Oliphant, T., & Peterson, P. (2014). SciPy: Open source scientific tools for Python.
- Kéfi, S., Rietkerk, M., Alados, Concepción L., Pueyo, Y., Papanastasis, V. P., ElAich, A., & De Ruiter, P. C. (2007). Spatial vegetation patterns and imminent desertification in Mediterranean arid ecosystems. *Nature*, 449(7159), 213.
- Kumar, B., Sreenivasulu, G., & Ramakrishna Rao, A. (2010). Metamodel-based design of alluvial channels at incipient motion subjected to seepage. *Hydrological Sciences Journal–Journal des Sciences Hydrologiques*, 55(3), 459–466. <https://doi.org/10.1080/02626661003741542>
- Larsen, L. G., Choi, J., Nungesser, M. K., & Harvey, J. W. (2012). Directional connectivity in hydrology and ecology. *Ecological Applications*, 22(8), 2204–2220. <https://doi.org/10.1890/11-1948.1>
- Lee, J. G., & Heaney, J. (2003). Estimation of urban imperviousness and its impacts on storm water systems. *Journal of Water Resources Planning and Management*, 129(5), 419–426. [https://doi.org/10.1061/\(ASCE\)0733-9496\(2003\)129:5\(419\)](https://doi.org/10.1061/(ASCE)0733-9496(2003)129:5(419))
- Leopold, L. (1968). Hydrology for urban land planning: A guidebook on the hydrological effects of urban land use, 18.

- Ludwig, J. A., Bastin, G. N., Chewings, V. H., Eager, R. W., & Liedloff, A. C. (2007). Leakiness: A new index for monitoring the health of arid and semiarid landscapes using remotely sensed vegetation cover and elevation data. *Ecological Indicators*, 7(2), 442–454. <https://doi.org/10.1016/j.ecolind.2006.05.001>
- Ludwig, J. A., Wilcox, B. P., Breshears, D. D., Tongway, D. J., & Imeson, A. C. (2005). Vegetation patches and runoff–erosion as interacting ecohydrological processes in semiarid landscapes. *Ecology*, 86(2), 288–297.
- Magliano, P. N., Breshears, D. D., Fernández, R. J., & Jobbágy, E. G. (2015). Rainfall intensity switches ecohydrological runoff/runon redistribution patterns in dryland vegetation patches. *Ecological applications*, 25(8), 2094–2100. <https://doi.org/10.1890/15-0550.1>
- Mapping, S. V., & LiDAR Program, University of Maryland (2016). Sonoma vegetation mapping and lidar products. <http://sonomavegmap.org/data-downloads/>
- Masselink, R. J., Heckmann, T., Temme, A. J., Anders, N. S., Gooren, H. P., & Keesstra, S. D. (2017). A network theory approach for a better understanding of overland flow connectivity. *Hydrological Processes*, 31(1), 207–220. <https://doi.org/10.1002/hyp.10993>
- Matsuki, K., Kuperman, V., & Van Dyke, J. A. (2016). The random forests statistical technique: An examination of its value for the study of reading. *Scientific Studies of Reading*, 20(1), 20–33. <https://doi.org/10.1080/10888438.2015.1107073>
- Mayor, Angeles G., Bautista, S., Small, E. E., Dixon, M., & Bellot, J. (2008). Measurement of the connectivity of runoff source areas as determined by vegetation pattern and topography: A tool for assessing potential water and soil losses in drylands. *Water Resources Research*, 44, W10423. <https://doi.org/10.1029/2007WR006367>
- Mügler, C., Planchon, O., Patin, J., Weill, S., Silvera, N., Richard, P., & Mouche, E. (2011). Comparison of roughness models to simulate overland flow and tracer transport experiments under simulated rainfall at plot scale. *Journal of Hydrology*, 402(1–2), 25–40. <https://doi.org/10.1016/j.jhydrol.2011.02.032>
- Neelakantan, T., & Pundarikanthan, N. (2000). Neural network-based simulation-optimization model for reservoir operation. *Journal of Water Resources Planning and Management*, 126(2), 57–64. [https://doi.org/10.1061/\(ASCE\)0733-9496\(2000\)126:2\(57\)](https://doi.org/10.1061/(ASCE)0733-9496(2000)126:2(57))
- Noy-Meir, I. (1979). Structure and function of desert ecosystems. *Israel Journal of Plant Sciences*, 28(1), 1–19.
- Okun, G. S., Heras, M. M.-dl., Saco, P. M., Throop, H. L., Vivoni, E. R., Parsons, A. J., et al. (2015). Connectivity in dryland landscapes: Shifting concepts of spatial interactions. *Frontiers in Ecology and the Environment*, 13(1), 20–27. <https://doi.org/10.1890/15-0550.1>
- Parr, T., Turgutlu, K., Csiszar, C., & Howard, J. (2018). Beware default random forest importances. <https://explained.ai/rf-importance/index.html>, accessed 12-December-2018.
- Paschalis, A., Katul, G. G., Faticchi, S., Manoli, G., & Molnar, P. (2016). Matching ecohydrological processes and scales of banded vegetation patterns in semiarid catchments. *Water Resources Research*, 52, 2259–2278. <https://doi.org/10.1002/2015WR017679>
- Pedregosa, F., Varoquaux, G., Gramfort, A., Michel, V., Thirion, B., Grisel, O., et al. (2011). Scikit-learn: Machine learning in Python. *Journal of Machine Learning Research*, 12, 2825–2830.
- Penny, G. G., Daniels, K. E., & Thompson, S. E. (2013). Local properties of patterned vegetation: Quantifying endogenous and exogenous effects. *Philosophical Transactions of the Royal Society A: Mathematical, Physical and Engineering Sciences*, 371(2004), 20120359.
- Razavi, S., Tolson, B. A., & Burn, D. H. (2012). Numerical assessment of metamodelling strategies in computationally intensive optimization. *Environmental Modelling & Software*, 34, 67–86. <https://doi.org/10.1016/j.envsoft.2011.09.010>
- Reaney, S., Bracken, L., & Kirkby, M. (2007). Use of the Connectivity of Runoff Model (CRUM) to investigate the influence of storm characteristics on runoff generation and connectivity in semi-arid areas. *Hydrological Processes: An International Journal*, 21(7), 894–906. <https://doi.org/10.1002/hyp.6281>
- Reynolds, J., Virginia, R., & Schlesinger, W. (1997). Defining functional types for models of desertification, *Plant functional types: Their relevance to ecosystem properties and global change* (Vol. 1, pp. 195). Cambridge: Cambridge University Press.
- Richards, L. A. (1931). Capillary conduction of liquids through porous mediums. *Physics*, 1(5), 318–333.
- Rietkerk, M., Boerlijst, M. C., van Langevelde, F., HilleRisLambers, R., de Koppel, J. v., Kumar, L., et al. (2002). Self-organization of vegetation in arid ecosystems. *The American Naturalist*, 160(4), 524–530.
- Rietkerk, M., Ketner, P., Burger, J., Hoorens, B., & Olf, H. (2000). Multiscale soil and vegetation patchiness along a gradient of herbivore impact in a semi-arid grazing system in west africa. *Plant Ecology*, 148(2), 207–224.
- Rogers, L. L., & Dowla, F. U. (1994). Optimization of groundwater remediation using artificial neural networks with parallel solute transport modeling. *Water Resources Research*, 30(2), 457–481. <https://doi.org/10.1029/93WR01494>
- Rohmer, J., Idier, D., Paris, F., Pedreros, R., & Louisor, J. (2018). Casting light on forcing and breaching scenarios that lead to marine inundation: Combining numerical simulations with a random-forest classification approach. *Environmental Modelling & Software*, 104, 64–80. <https://doi.org/10.1016/j.envsoft.2018.03.003>
- Schueler, T., Fraley-McNeal, L., & Cappiella, K. (2009). Is impervious cover still important? review of recent research. *Journal of Hydrologic Engineering*, 14(4), 309–315. [https://doi.org/10.1061/\(ASCE\)1084-0699\(2009\)14:4\(309\)](https://doi.org/10.1061/(ASCE)1084-0699(2009)14:4(309))
- Shuster, W. D., Bonta, J., Thurston, H., Warnemuende, E., & Smith, D. R. (2005). Impacts of impervious surface on watershed hydrology: A review. *Urban Water Journal*, 2(4), 263–275. <https://doi.org/10.1080/15730620500386529>
- Simunek, J., Van Genuchten, M. T., & Sejna, M. (2005). The HYDRUS-1D software package for simulating the one-dimensional movement of water, heat, and multiple solutes in variably-saturated media. *University of California-Riverside Research Reports*, 3, 1–240.
- Smith, M. W., Cox, N. J., & Bracken, L. J. (2007). Applying flow resistance equations to overland flows. *Progress in Physical Geography: Earth and Environment*, 31(4), 363–387. <https://doi.org/10.1177/0309133307081289>
- Sreekanth, J., & Datta, B. (2010). Multi-objective management of saltwater intrusion in coastal aquifers using genetic programming and modular neural network based surrogate models. *Journal of Hydrology*, 393(3–4), 245–256. <https://doi.org/10.1016/j.jhydrol.2010.08.023>
- Stavi, I., Rachmilevitch, S., & Yizhaq, H. (2018). Small-scale geodiversity regulates functioning, connectivity, and productivity of shrubby, semi-arid rangelands. *Land Degradation & Development*, 29(2), 205–209. <https://doi.org/10.1002/ldr.2469>
- Thompson, S., Harman, C., Heine, P., & Katul, G. (2010). Vegetation-infiltration relationships across climatic and soil type gradients. *Journal of Geophysical Research*, 115, G02023. <https://doi.org/10.1016/j.advwatres.2011.05.012>
- Thompson, S., Katul, G., Konings, A., & Ridolfi, L. (2011). Unsteady overland flow on flat surfaces induced by spatial permeability contrasts. *Advances in water resources*, 34(8), 1049–1058. <https://doi.org/10.1016/j.eharsci.2013.02.001>
- Tongway, D. J., & Ludwig, J. A. (2001). Theories on the origins, maintenance, dynamics, and functioning of banded landscapes, *Banded vegetation patterning in arid and semiarid environments* (pp. 20–31). New York, NY: Springer.
- Turnbull, L., Hütt, M.-T., Ioannides, A. A., Kininmonth, S., Poepl, R., Tockner, K., et al. (2018). Connectivity and complex systems: Learning from a multi-disciplinary perspective. *Applied Network Science*, 3(1), 11. <https://doi.org/10.1002/eco.1806>
- Turnbull, L., & Wainwright, J. (2019). From structure to function: Understanding shrub encroachment in drylands using hydrological and sediment connectivity. *Ecological Indicators*, 98, 608–618.

- Turner, M. G. (1989). Landscape ecology: The effect of pattern on process. *Annual Review of Ecology and Systematics*, 20(1), 171–197. <https://doi.org/10.1146/annurev.es.20.110189.001131>
- Van Genuchten, M. T. (1980). A closed-form equation for predicting the hydraulic conductivity of unsaturated soils 1. *Soil science society of America journal*, 44(5), 892–898. <https://doi.org/10.2136/sssaj1980.03615995004400050002>
- Yan, S., & Minsker, B. (2003). A dynamic meta-model approach to genetic algorithm solution of a risk-based groundwater remediation design model. In *World water & environmental resources congress 2003* (pp. 1–10). Salt lake City. [https://doi.org/10.1061/40685\(2003\)99](https://doi.org/10.1061/40685(2003)99)